Modeling the hot flow behavior of a Fe-22Mn-0.41 C-1.6Al-1.4Si TWIP steel microalloyed with Ti, V and Nb

I. Mejía, F. Reyes-Calderón, J.M. Cabrera

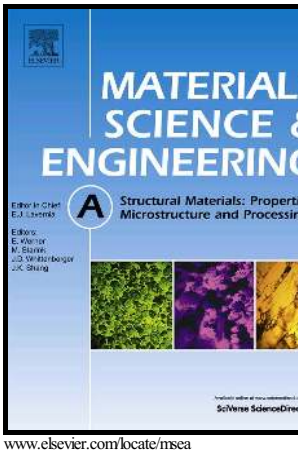

www.elsevier.com/locate/msea

PII: S0921-5093(15)30228-8
DOI: http://dx.doi.org/10.1016/j.msea.2015.07.078
Reference: MSA32616

To appear in: *Materials Science & Engineering A*

Received date: 17 December 2014
Revised date: 21 July 2015
Accepted date: 24 July 2015

Cite this article as: I. Mejía, F. Reyes-Calderón and J.M. Cabrera, Modeling the hot flow behavior of a Fe-22Mn-0.41 C-1.6Al-1.4Si TWIP steel microalloyed with Ti, V and Nb, *Materials Science & Engineering A* http://dx.doi.org/10.1016/j.msea.2015.07.078

Modeling the hot flow behavior of a Fe-22Mn-0.41C-1.6Al-1.4Si TWIP steel microalloyed with Ti, V and Nb

I. Mejía[a, *], F. Reyes-Calderón[a,b], J.M. Cabrera[c,d]

[a] Instituto de Investigaciones Metalúrgicas,
Universidad Michoacana de San Nicolás de Hidalgo.
Edificio "U", Ciudad Universitaria, 58066-Morelia, Michoacán, México.

[b] Departamento de Metalmecánica,
Instituto Tecnológico de Morelia.
Av. Tecnológico 1500, 58120-Morelia, Michoacán, México.

[c] Departament de Ciència dels Materials i Enginyeria Metal·lúrgica,
ETSEIB – Universitat Politècnica de Catalunya.
Av. Diagonal 647, 08028-Barcelona, Spain.

[d] Fundació CTM Centre Tecnològic.
Plaza de la Ciencia, 2, 08243-Manresa, Spain.

[*] Corresponding author. Tel.: +52 (443) 322 3500 Ext: 4034; Fax: +52 (443) 322 3500 Ext: 4010. E-mail address: imejia@umich.mx, i.mejia.granados@gmail.com

Abstract

The present research work analyses the influence of Ti, V and Nb microalloying elements on the hot flow behavior of a high-Mn TWIP (Twinning Induced Plasticity) steel. For this purpose, flow curves were obtained by uniaxial hot compression tests performed at four strain rates (10^{-1}, 10^{-2}, 10^{-3} and 10^{-4} s^{-1}) and three temperatures (900, 1000 and 1100 ºC). The models of Estrin, Mecking and Bergstrom; Avrami and Tegart, and Sellars were applied to determine the hot working constants used to derive the constitutive equations describing the flow curves. The analysis of modeling parameters of the hot flow curves shows that Ti, V and Nb additions to TWIP steel generated slight increase in the peak stress (σ_p), retardation of the dynamic recrystallization (DRX) onset, particularly at low temperature, and decrease in the activation energy required to recrystallization (Q_t). Likewise, the softening effect promoted by DRV and DRX was more evident at high temperatures and low strain rates. On the other hand, the resulting deformed microstructures, analyzed by the SEM-EBSD technique, showed that the most important refining effect on recrystallized austenitic grain was in the presence of V and Ti. The good agreement between the experimental and predicted hot flow curves demonstrated that the developed constitutive equations predict with reasonable accuracy the hot flow behavior of the studied TWIP steels.

Keywords: Twinning induced plasticity (TWIP) steel; Ti, V and Nb microalloying elements; Hot flow behavior; Dynamic recrystallization (DRX); Constitutive equations.

Nomenclature

Q_{rec}	Activation energy for DRX.
Q_{HW}	Activation energy for hot working.
Q	Activation energy required into the deformation process.
Q_t	Activation energy required to recrystallization.
a, b	Avrami constants.
n_g	Avrami exponent calculated for every test condition.
n_A	Avrami exponent.
b	Burgers vector.
n	Creep exponent.
K_D	Derby's coefficient.
n_D	Derby's exponent.

ρ	Dislocations density.
X	Dynamically recrystallized volume fraction.
ρ_0	Initial dislocations density.
d_0	Initial grain size.
α	Inverse of the stress associated with power-law breakdown.
α_a	Material constant due to DRV.
A	Material constant due to steady state stage.
A_p, α_p, A_{ss}, α_{ss}	Material constants correspondent to the peak stress and steady state.
$k_{t50\%}$, $m_{t50\%}$	Material constants related to 50% of recrystallization.
k_t, m_t, n_t	Material constants related to recrystallization.
K_ε, m_ε, $n_{\varepsilon,}$ $m_{\sigma p}$	Material constants.
T_m	Melting temperature.
K_Ω, m_Ω, K_U, m_U	Modeling constant values.
ε_p	Peak strain.
σ_p	Peak stress.
ε	Plastic strain.
d_{rec}	Recrystallized grain size.
σ_s	Saturation stress.
μ_o	Shear modulus.
Ω	Softening due to DRV.
σ_{ss}	Steady state stress.
$\dot{\varepsilon}$	Strain rate.
$(\sigma_p(T)/E(T))$	Temperature dependent stress normalized by the temperature dependent Young modulus.
$D_{Fe}^{\gamma}(T)$	Temperature dependent γ-Fe lattice self-diffusion coefficient.
T	Test temperature.
$t_{50\%}$	Time necessary for 50% of recrystallization.
t	Time.
ε_t	True strain.
σ_t	True stress.
R	Universal gas constant.
U	Work hardening due to DRV.
Z	Zener-Hollomon parameter.
A-UHSS	Advanced ultra-high strength steels.
BC	Band contrast.
CSL	Coincidence site lattice.
DRV	Dynamic recovery.
DRX	Dynamic recrystallization.

GAM	Grain average misorientation.
GB	Grain boundaries.
KJMA	Kolmogorov-Johnson-Mehl-Avrami Model.
RF	Recrystallized fraction.
SEM-EBSD	Scanning Electron Microscopy-Electron Backscattering Diffraction.
SFE	Stacking Fault Energy.

1. Introduction

High-Mn TWIP steels provide a great potential to the manufacturing, building and automotive industries **[1-6]**. There are several studies **[1-5]** about the chemical compositions of TWIP steels and their influence on the deformation mechanisms, the mechanical properties, the stacking fault energy (SFE) and the phase transformations during cold deformation processes. However, there are few researches about the hot flow behavior **[6-14]**. These studies show, as expected, the influence of temperature (T), plastic deformation or strain (ε) and strain rate ($\dot{\varepsilon}$) on the hot flow behavior. Nevertheless, less effort has been addressed to perform a good control of these parameters to obtain an optimal microstructural conditions and therefore to promote their mechanical properties.

Hot compression tests are usually carried out to simulate industrial processes such as forging, rolling, extrusion, etc. The obtained hot flow curves (σ_t-ε_t) show the typical plastic behavior of steels at high temperature, *i.e.*, a single peak in the flow stress is noticed. The flow curves are furthermore characterized by three distinctive zones: *i*) A stage I that is related to the balance between the generated and the stored dislocations by strain hardening, together with those rearranged and annihilated by dynamic recovery (DRV) **[15, 16]**. *ii*) A stage II extends from the peak stress (σ_p) to the steady state stress (σ_{ss}). This stage represents the progress of an additional softening mechanism called dynamic recrystallization (DRX), which can be modeled by the classical equations proposed by Kolmogorov-Johnson-Mehl-Avrami (KJMA) **[17-21]** assuming that the stress softening is proportional to the recrystallized volume fraction (X), and *iii*) A stage III where the metal attains an ideal plastic flow behavior that can be modeled by using the Sellars and Tegart equations **[22]**, modified by Cabrera *et al.* **[23]** by including a correction of the Young modulus dependence on temperature.

The appropriate design of the thermo-mechanical treatment is important in simulating hot forming processes, in order to control the grain size during the hot deformation. This is particularly true in TWIP steels **[10]**, where no phase transformations occurs during cooling. Additionally, the austenitic grains can be further refined by a fine dispersion of particles randomly distributed within the matrix. In this case, particles must be sufficiently stable to not dissolve or to not grow during the reheating and hot forming operations **[24]**. The addition of microalloying elements such as Nb and Ti can promote an extra strengthening via precipitation hardening or via grain refinement in high-Mn steels, and the imminent production of finer grain sizes at the end of the steel processing as previously was reported by Dobrzanski *et al.* **[10]**. Additionally, they reported **[11]** that the relative low strain values (ε_p) to initiate DRX produce a more refined austenitic microstructure after multiple deformation passes because the earlier activation of DRX. On the other hand, Hamada *et al.* **[6]** reported that increasing the Al content in TWIP steels is possible to change the ε_p values from 0.17 to 0.28, with a consequent retardation on the DRX onset.

The present work analyzes from experimental true stress-strain data of uniaxial hot compression tests performed at three different temperatures and four strain rates, the separate effect of microalloying elements (Nb, V and Ti) on the hot flow behavior of a high-Mn TWIP steel. Additionally, mathematical modeling of the hot flow curves has been carried out by using previous models and equations obtained from scientific literature **[23, 25-41]**, which are summarized as follows.

2. Constitutive models to the hot flow behavior

As already pointed out, previous research works **[23, 25-41]** have established constitutive models from experimental data to describe and predict the hot flow behavior during the thermo-mechanical processing. The models analyze separately the three stages above described of the hot flow curves. In the stage I, strain hardening and DRV are the dominant mechanisms, and the so-called one variable approach model can be used **[15, 16]**. It states that during hot deformation, the dependence of the dislocation density (ρ) on plastic strain (ε) is generally considered to be a balance between dislocations generated by work hardening and dislocations annihilated by DRV, resulting in the following equation:

$$\frac{\partial \rho}{\partial \varepsilon} = U - \Omega\rho \quad (1)$$

where U represents the work hardening and Ω is the softening due to DRV. This expression has already been used in a wide range of materials **[16, 23, 25, 28, 29]** and its integration is relatively simple assuming that both U and Ω are independent of strain (ε). Assuming the classical relationship between the stress and dislocation density (ρ):

$$\sigma = \alpha_a \cdot \mu_0 \cdot b \cdot \sqrt{\rho} \quad (2)$$

where α_a is a material constant, μ_0 is the shear modulus and b the Burgers vector, then, **Eq.** (**1**) becomes in the following constitutive expression:

$$\sigma^2 = \sigma_0^2 e^{-\Omega\varepsilon} + \sigma_s(1 - e^{-\Omega\varepsilon}) \quad (3)$$

being $\sigma_0 = \alpha_a \mu b\sqrt{\rho_0}$ and $\sigma_s = \alpha_a \mu b\sqrt{U/\Omega}$, where ρ_0 is the initial dislocation density. Here σ_s is the saturation stress, *i.e.*, the stress in the absence of DRX, equal to σ_{ss} in the case of softening solely by DRV, and very close to peak stress (σ_p) in the presence of DRX. For the determination of the constitutive equations it is necessary to establish the influence of the strain rate ($\dot{\varepsilon}$) and temperature (T) on σ_p, U and Ω.

The stage II is controlled by the DRX process. As any process of solid state transformation that takes place by nucleation and growth, DRX has a kinetic that can be modeled by the classical Kolmogorov-Johnson-Mehl-Avrami (KJMA) equation **[17-21]**:

$$X = 1 - exp(-kt^{n_A}) \quad (4)$$

where X is the dynamically recrystallized volume fraction in a given period of time (t), and n_A and k are the constants related to the nucleation and growth rate mechanism, respectively. If the peak strain (ε_p), the strain rate ($\dot{\varepsilon}$) and the progressing strain (ε) are known, then:

$$t = \frac{\left(\varepsilon - \varepsilon_p\right)}{\dot{\varepsilon}} \tag{5}$$

The time for 100% DRX may stabilize at low slope, which would increase the error while calculating the constant k. Hence, it is customary to define the recrystallization kinetics in terms of the time for 50% of recrystallization ($t_{50\%}$). Since $exp(-0.693) \approx 0.5$, the relationship between $t_{50\%}$ and the constant k can be expressed as:

$$t_{50\%} = \left(\frac{0.693}{k}\right)^{1/n_A} \tag{6}$$

It has been experimentally verified **[42, 43]** that $t_{50\%}$ depends on the deformation parameters, such as temperature (T), strain rate ($\dot{\varepsilon}$) and initial grain size (d_0) as follows:

$$t_{50\%} = k_t \cdot \dot{\varepsilon}^{m_t} \cdot d_0^{n_t} \cdot exp\left(\frac{Q_{rec}}{RT}\right) \tag{7}$$

where k_t, m_t and n_t are material constants, Q_{rec} is an activation energy (driving force) for DRX and R is the universal gas constant. Combining the **Eqs.** (**4**) and (**6**), the recrystallized fraction can be expressed as **[23]**:

$$X = 1 - exp\left(-0.693\left(\frac{\varepsilon - \varepsilon_p}{\dot{\varepsilon} \cdot t_{50\%}}\right)^{n_A}\right) \tag{8}$$

Finally, it is assumed that X is proportional to the stress softening:

$$X = \frac{\sigma_p - \sigma}{\sigma_p - \sigma_{ss}} \tag{9}$$

Therefore, the flow curve under DRX conditions can be expressed as:

$$\sigma = \sigma_p - (\sigma_p - \sigma_{ss})\left[1 - exp\left(-0.693\left(\frac{\varepsilon - \varepsilon_p}{\dot{\varepsilon} \cdot t_{50\%}}\right)^{n_A}\right)\right] \quad (10)$$

where σ_{ss} is the steady state stress attained at large strains as already pointed out. This equation is only valid for $\varepsilon > \varepsilon_p$. In general, the use of **Eqs.** (**3**), (**7**) and (**10**) in conjunction with some additional kinetic equations that will be shown in the next paragraph will allow modeling the experimental hot flow curves, whether or not DRX is occurring.

Finally, the stage III is completed with the determination of the kinetic equation for the steady-state stress, which can be also be applied to the peak stress. For this purpose, the hyperbolic sine law is traditionally applied **[22, 28, 44]**:

$$\dot{\varepsilon} = A[\sinh(\alpha\sigma)]^n \cdot exp\left(\frac{-Q}{RT}\right) \quad (11)$$

where A is a material constant, n is the creep exponent and α is the inverse of the stress associated with power-law breakdown. Although the constants A, n, α and the activation energy required into the deformation process (Q) depend on the material considered, they are referred as apparent values **[23]**. When the initial grain size and the dependence of Young modulus on temperature are taken into account, a constant creep exponent $n = 5$ and the self-diffusion activation energy for γ-Fe (Q=270,000 J/mol) **[45]** can be used to describe the σ_p behavior. The unified expression is defined as follows:

$$\frac{\dot{\varepsilon}}{D_{Fe}^{\gamma}(T)} = A_p\left[\sinh\left(\frac{\alpha_p \sigma_p}{E(T)}\right)\right]^5 \quad (12)$$

In this equation, the temperature dependent stress is normalized by the temperature dependent Young's modulus ($\sigma_p(T)/E(T)$) and also the strain rate is normalized by the γ-Fe lattice self-diffusion coefficient (D_{Fe}^{γ} (T)). In this case, the diffusion coefficient and Young's modulus as a function of the temperature **[45]** are defined as:

$$D_{Fe}^{\gamma}(T) = 1.6 \cdot 10^{-4}\ exp\left(-\frac{270{,}000}{RT}\right) \quad (13)$$

and

$$E(T) = 2.66\mu_0 \left[1 + \left(\frac{T - 300}{T_m}\right)\left(\frac{T_m d_\mu}{\mu_0 dT}\right)\right] \quad (14)$$

where μ_0 is the shear modulus, T_m is the melting temperature and the term ($T_m d_\mu/\mu_0 dT$) is the dimensionless coefficient of temperature dependence of shear modulus, as proposed by Frost and Ashby **[45]**.

3. Experimental procedure

Four TWIP steels were melted in the Foundry Lab of the IIM-UMSNH, México. A non-microalloyed TWIP steel (TW-NM) and other three single microalloyed with Nb (TW-Nb), V (TW-V) and Ti (TW-Ti). The chemical compositions are listed in **Table 1**. Rectangular samples (75 x 60 x 25 mm) were homogenized at 1200 ºC for 5 h and then hot rolled up to 60% thickness reduction. Samples were then subjected to a solution heat treatment at 1200 ºC for 1 h and water quenched at room temperature, in order to promote a similar initial solution condition of the austenitic grains in the studied TWIP steels. As shown in **Fig. 1**, the average initial grain sizes determined by the general intercept procedure of the standard test method proposed by ASTM E 112-96 **[46]** were 104±23 μm for TW-NM, 112±12 μm for TW-Nb, 129±16 μm for TW-V and 63±32 μm for TW-Ti steels.

Cylindrical samples (7 mm in diameter x 11 mm in length) were machined using electric discharging machining (EDM). Uniaxial hot compression tests were carried out in an Instron machine coupled with a radiant cylindrical furnace and using inert atmosphere of Ar at three temperatures (900, 1000 and 1100 ºC) and four constant strain rates (10^{-1}, 10^{-2}, 10^{-3} and 10^{-4} s^{-1}). The heating rate was 10 ºC/s. Samples were kept for 10 min at the soaking temperatures for homogenization purposes before the hot compression. The temperature control was performed by a K-type thermocouple placed on the sample surface. Two tantalum thin foils and boron nitride were used as lubricants to minimize the friction and the subsequent barreling effect of the specimen. The total strain was of ε = 0.8, and according to previous results **[47]** no correction was made of the flow curves due to friction. An adiabatic correction was not necessary, because the strain rates involved were not very large **[47]**. A specific device coupled to the testing machine was designed to quench specimens in water immediately (less

than 0.5 s), in order to retain the recrystallized microstructure. The mathematical data processing was performed in the software Origin 8.0©. The metallographic preparation was done using the conventional techniques of grinding and polishing up to diamond paste of 1μm. The final polishing was performed with colloidal silica of 0.05 μm for 1 h at constant pressure and speed (150 $N \cdot m^2$ and 200 rpm). Hot deformed microstructures were analyzed by light optical microscopy (LOM) and SEM-EBSD techniques. Images with band contrast (BC), grain boundaries (GB), coincidence site lattices (CSL) and the recrystallized fractions (RF) were obtained. Data processing was done with the software Channel 5© (HKL Technology).

4. Results and discussion

4.1. Experimental hot flow curves

Fig. 2 shows the experimental hot flow curves obtained. All flow curves are of the single peak type. At low strain rate (10^{-4} s^{-1}) and low temperatures (900 and 1000 ºC), as shown in **Figs. 2** (**a**, and **b**), there is no effect of the chemical composition on the hot flow behavior, *i.e.*, σ_p and ε_p values were similar in all TWIP steels. When temperature rises up to 1100 ºC and the strain rate is 10^{-4} s^{-1} (**Fig. 2**(**c**)), the σ_p values are higher for the microalloyed TWIP steels than in the non-microalloyed TWIP steel, but a reduction of the ε_p values is also experienced. The TW-NM steel at this condition shows the lowest σ_p value of all tested steels. Finally, **Figs. 2** (**a**, **d**, **g**, and **j**) show a slight increase of the σ_p value for microalloyed TWIP steels tested at 900 ºC.

4.2. Modeling the hardening and recovery stages

As previously mentioned, **Eq.** (**2**) allows the calculation of U and Ω parameters of the stage I. Assuming $\sigma_0 = 0$ and using a least square method to fit experimental data to **Eq.** (**2**), the hardening (U) and softening (Ω) terms were derived and plotted as a function of the Zener-Hollomon parameter (Z), *i.e.*, the strain rate is compensated by temperature, which in turn is defined as follows:

$$Z = \dot{\varepsilon} \cdot exp\left(\frac{Q_{HW}}{RT}\right) \quad (15)$$

where Q_{HW} is the activation energy for hot working, which were previously calculated **[48]** for the present TWIP steels (Q_{TW-NM} = 366, Q_{TW-Nb}= 434, Q_{TW-V} = 446 and Q_{TW-Ti} = 425 kJ/mol), T is the deformation temperature, $\dot{\varepsilon}$ is the strain rate and R is the universal gas constant (8.314 J/mol·K). As shown in **Fig. 3**, a potential relationship between both terms and Z can be easily noticed, responding to the following mathematical relationships:

$$\Omega = K_{\Omega} \cdot Z^{m_{\Omega}} \tag{16}$$

$$(\alpha' \mu b)^2 \cdot U = K_{U} \cdot Z^{m_{U}} \tag{17}$$

Experimental values of Ω and U were also fitted by the least-square method to **Eqs.** (**16**) and (**17**). Then, the modeling constant values (K_{Ω}, m_{Ω} and K_{U}, m_{U}) were obtained. **Fig. 3**(**a**) also shows the dependence of the softening term (Ω) of the analyzed TWIP steels on the chemical composition, *i.e.*, the parameter Ω depends on the microalloying elements. The TW-Ti steel displays the highest Ω exponent (in absolute values). It is worth mentioning that the softening term is also higher for the TW-Ti steel at low Z values, followed by the TW-V and TW-Nb. However, this behavior is the opposite at high Z values, where the TW-Nb steel shows the highest softening.

A similar procedure was used to calculate U (**Fig. 3**(**b**)). In this case, the highest m_{U} exponent is observed in the TW-Nb steel, followed by the TW-V and TW-Ti steel, respectively. The highest hardening term is observed in the TW-V steel, followed by the TW-Ti and TW-Nb, irrespective of the Z value considered, although at the highest Z values all three steel seems to offer similar hardening values, *i.e.*, the chemical composition does not affect the hardening term at the highest strain rate and the lowest temperature.

4.3. Modeling the dynamic recrystallization (DRX) stage

The ε_p values were obtained directly from the experimental data, which correspond to the maximum stress value for each flow curve. These values are commonly associated, for simplification purposes, to the DRX onset. On the other hand, ε_p depends on the deformation temperature, the strain rate and the initial grain size as a power function of the form:

$$\varepsilon_p = K_\varepsilon \cdot d_0^{n_\varepsilon} \cdot Z^{m_\varepsilon} \quad (18)$$

where K_ε, n_ε and m_ε are material constants, d_0 is the initial grain size and Z is the Zener-Hollomon parameter. If d_0 remains constant, as in this case of microalloyed TWIP steels, **Eq. (18)** can be simplified to:

$$\varepsilon_p = K_\varepsilon \cdot Z^{m_\varepsilon} \quad (19)$$

The experimental relationships of σ_p and ε_p respect the Zener-Hollomon parameter (Z) are shown in **Fig. 4**. As can be seen, DRX is a thermally activated phenomenon and the amount of stress and deformation necessaries to the DRX onset are proportional to Z values **[49]**. Microalloying elements in TWIP steels produced a slight increase on σ_p values, as can be seen in **Fig. 4(a)**. It is evident that σ_p values increase either at high strain rates or when test temperature is low. This in turn means that the higher the Z values the higher the stress required to the DRX onset. Then, it was possible to determine the influence of microalloying elements on the σ_p necessary to the DRX onset. **Fig. 4(a)** shows how at high temperatures or low strain rates there is a slight deviation on the σ_p values, and the lowest value is for TW-NM. On the other hand, the highest σ_p value at high Z value is for TW-Nb, although the deviation respect to other TW steels is minimal. As a result of this analysis, the slope of the predicted values represented as the exponent ($m_{\sigma p}$) is close to 0.15 for all analyzed TWIP steels. Such value is a little bit lower than the typical stress exponent (0.2) which is an indication of some extra-hardening promoted by precipitated particles. When the deformation mechanism is only governed by the glide and climb of dislocations such exponent should be close to 0.2. A diminution of this value typically indicates some precipitation hardening, which in the present case is at the most, very minor. It is worth noting that particles are even present in the TW-NM steel in the form of aluminum nitrides. The most important effects on σ_p and ε_p are shown in TW-Ti and TW-V steels, particularly at low Z values. In **Fig. 4(b)** it is possible to appreciate how the V and Nb presence reduces the ε_p values. Therefore, the DRX onset is slightly accelerated in TW-V steel.

4.4. Dynamic recrystallization (DRX) kinetics

The Avrami relationship showed in **Eq.** (**4**) and the KJMA model **[17-21]** allows the calculation of the DRX kinetics. Taking into account that the onset of DRX is considered as the ε_p value, the softening stage is limited by the (σ_p) value and the beginning of the steady state stress (σ_{ss}). Thus, the recrystallized fraction (X) is derived from **Eq.** (**9**).

The results in **Fig. 5**(**a**) show that, the DRX kinetics retardation is due to the microalloying presence such as Ti, but it produces an acceleration of the DRX onset. Microalloying elements delay the DRX, therefore the recrystallization process is delayed too. Traditionally, the Avrami exponent (n_A) is determined by using a linear data fitting and measuring the slope of the double logarithmic plot ln(ln(1/(1-X))) vs. ln((ε-ε_p)/$\dot{\varepsilon}$), as can be seen from **Fig. 5**(**a**). The Avrami exponent is considered constant and independent of the test conditions **[50, 51]**. Possible changes of these values are associated with saturation of the available sites for nucleation, which can be vertices, edges and surfaces of the grain boundaries, reaching values between 1 and 2 **[23, 25, 28, 29, 52-54]** for the nucleation of new grains dynamically recrystallized in austenite grain boundaries. These conditions were observed in the four analyzed TWIP steels. As an example, **Fig. 5**(**a**) shows the TW-NM steel at 900°C, where it is unclear the dependence of the Avrami exponent calculated for every test condition (n_g) with the strain rate or temperature, as previously determined by Porter *et al.* **[50]** and Christian **[51]**. Therefore, the following average Avrami exponent (n_A) values for TW steels were obtained from calculations of averaged n_g values at 900, 1000 and 1100 °C, respectively: $n_{A(TW\text{-}NM)}$ = 1.21, $n_{A(TW\text{-}Nb)}$ = 1.05, $n_{A(TW\text{-}V)}$ = 1.98 and $n_{A(TW\text{-}Ti)}$ = 2.35. The obtained values ($1 \leq n \leq 2$) for TW-NM, TW-Nb and TW-V steels are in good agreement when nucleation sites correspond to grain boundaries. In these sites there is a high nuclei density to prevent the grain growth when they are touched by neighbors grains, producing grain refinement **[55]**. The value of $n_{A(TW\text{-}Ti)}$ = 2.35 is in accordance with the theory that the available sites for nuclei have a random distribution **[56]**, which is represented for the nonlinearity of the Avrami plot (highly dispersed values) in **Fig. 5**(**b**). These analyses also corroborate the grain refinement produced by single peak flow curves obtained to the four TWIP steels of this work. The low dependence of n_A on temperature and strain rate showed in **Fig. 5**(**b**) can be expressed by the following fit:

$$n_A = a + b \cdot log\, Z \tag{20}$$

As already mentioned, the recrystallized volume fraction (X) is assumed proportional to the softening observed in the flow curve. This in turn is considered to calculate the time necessary to produce 50% of recrystallized volume ($t_{50\%}$). If the initial grain size (d_0) is kept constant as assumed in the present research work, **Eq.** (**7**) can be simplified as follows:

$$t_{50\%} = k_{t50\%} \cdot \dot{\varepsilon}^{m_{t50\%}} \cdot exp\left(\frac{Q_t}{RT}\right) \tag{21}$$

The determined $t_{50\%}$ values were fitted using **Eq.** (**21**), and applying the least squares method the parameters $k_{t50\%}$, $m_{t50\%}$ and Q_t were obtained, which are listed in **Table 2**. Then, the time necessary for 50% recrystallization for analyzed TWIP steels are: $t_{50\%(TW\text{-}NM)}$ = 11.09 s, $t_{50\%(TW\text{-}Nb)}$ = 2.7 s, $t_{50\%(TW\text{-}V)}$ = 3,067.27 s, and $t_{50\%(TW\text{-}Ti)}$ = 2,274.81 s. As can be seen from **Table 2**, the $m_{t50\%}$ values are close in the four TWIP steels. There are no previous values for $m_{t50\%}$ reported in scientific literature for TWIP steels. However, compared with other low carbon steels microalloyed with boron **[25]**, advanced ultra-high strength steels (A-UHSS) microalloyed with boron **[49]** and medium carbon microalloyed steels **[23]**, the values obtained are slightly above. It is worth noting that at elevated temperatures twinning is reduced, however, the dislocation slip is always one of the dominating defects **[57, 58]**. According to Steinmetz *et al.* **[59]** temperature clearly delays the onset of twinning by simultaneously decreasing the flow stress, increasing the rate of dislocation annihilation through climb and increasing the SFE, which in turn increases the critical stress needed to initiate deformation twinning. They also determined that at elevated temperatures the effective shear stress never reaches the critical twinning stress. This change influences directly the microstructure, texture, work hardening and mechanical properties **[60]**. On the other hand, it is remarkably that $k_{t50\%}$ values are considerably higher for microalloyed TWIP steels than in TW-NM steel. This indicates that DRX kinetics is faster in TW-NM steel. Additionally, the activation energy (Q_t) required to start the DRX is higher in TW-NM than in microalloyed TWIP steels. Again, there are no previous reference values of $k_{t50\%}$ and Q_t for TWIP steels, but compared with boron microalloyed and medium carbon microalloyed steels previously mentioned, the calculated values present are lower.

4.5. Modeling the peak stress (σ_p) and steady-state stress (σ_{ss})

The final modeling stage is completed with the determination of kinetic equations for the peak stress (σ_p) and the steady-state stress (σ_{ss}), **Eqs.** (**11**) to (**14**). In these equations, the constant value $1.6x10^{-4}$ m^2/s corresponds to the self-diffusion coefficient of γ-Fe **[45]**, μ_0 is the shear modulus at 27 ºC ($8.31x10^4$ MPa), T_m is the melting temperature of TWIP steels (1400 ºC) and the constant term ($T_m d_\mu/\mu_0 dT$) is -0.91 for γ-Fe. The values of A and α constants for TWIP steels obtained on the basis of **Eq.** (**12**) for σ_p are plotted in **Fig. 6**(**a**).

The dependence of σ_{ss} on strain rate and temperature, as well as the corresponding values of A and α are shown in **Fig. 6**(**b**). The creep exponent was fixed at n = 5 in the four analyzed TWIP steels, *i.e.*, it was assumed that the deformation mechanism was controlled by the glide and climb of dislocations. When the $(\dot{\varepsilon}/D_{Fe}^{\gamma}(T))^{1/5}$ vs. ($\sigma_p/E(T)$) plot is presented in **Fig. 6**(**a**), it is possible to appreciate a good alignment and fitting using the hyperbolic sine equation. The same behavior is shown in the $(\dot{\varepsilon}/D_{Fe}^{\gamma}(T))^{1/5}$ vs. ($\sigma_{ss}/E(T)$) plot in **Fig. 6**(**b**). The same fitting behavior and correlation coefficient values were obtained in both non-microalloyed and microalloyed TWIP steels. It is worth mentioning that values of constant A cannot be related with test conditions, as previously mentioned by Cabrera *et al.* **[23]**. It only depends on the nature of the material considered. In this case, A is an apparent value because the internal microstructure of analyzed TWIP steels was not considered. In the case of the A_p constant obtained in relation with σ_p, the highest value is for TW-Nb steel while the lowest value is for TW-V steel (**Fig. 6**(**a**)). In reference to the A_{ss} constant related to σ_{ss}, the highest value is for TW-Nb steel while the lowest value is for TW-Ti steel (**Fig. 6**(**b**)). In contrast, α_p and α_{ss} values of TW-Nb steel are the lowest of the studied TWIP steels for both calculations (σ_p and σ_{ss}). The good agreement between experimental and estimated data for σ_p and σ_{ss} support the hypothesis **[23]** that there is no significant precipitation during hot compression and the proper use of the stress exponent (n = 5).

4.6. Validation of the model and constitutive equations

The constitutive equations to the hot flow behavior of the studied TWIP steels were solved by substitution of the calculated parameters in the above procedure, which are shown in **Table 3**. Those parameters were evaluated at the strain range (ε_t = 0 to 0.8) used in the experimental tests, in order to be compared with the predicted behavior, as shown in **Figs. 7** (**a-l**). It is

possible to see that the model has a good agreement to the experimental data. However, there are some deviations in tests performed at high temperature and high strain rate (1100 ºC and 10^{-1} s^{-1}), as shown in **Figs. 7**(**f**, **i**, and **l**)). These deviations are associated to several experimental causes, *e.g.,* experimental errors because of the high strain rate test and the slow machine response. Additionally, it is important to take into account that theoretical curves consider an isothermal test, but experimental test are realized with adiabatic heating, which produces a higher heating than the expected one.

It is important to mention that previous research works have widely studied the Nb effect, in order to analyze its influence on processing parameters as shown in Table 3. Cuddy **[61, 62]** determined that in microalloyed Nb steel, the presence of Nb carbide and carbonitride postponed coarsening to higher temperatures, the austenite recrystallization and growth presumably by particle pinning of grain boundaries. But, an abrupt abnormal growth occurred between 1100 to 1150°C producing a duplex austenite structure. Nevertheless, at certain compositional Nb variations there is no effect on precipitation, boundary pinning and grain flattering at high temperatures, because of the interaction of dissolution kinetics, precipitation kinetics and precipitation growth at high temperatures **[63]**. Vervynckt *et al.* **[64]** and Speer *et al.* **[65]** confirmed that Nb can retard static recrystallization (SRX) of austenite at low temperatures by solute drag or by precipitation pinning in HSLA steels and low carbon steels, respectively. Additionally, their results indicated that Nb as precipitate is more effective in retarding the recrystallization than Nb in solid solution, and recrystallization becomes faster when the volume fraction of precipitates is reduced and/or precipitated coarsening rate is increased. Recrystallization kinetics curves for newly elaborated microalloyed steels have been determined by Opiela *et al.* **[66]**. They concluded that the impact of alloying elements Nb, Ti and V, dissolved in a solid solution and the presence of dispersive particles of MX-type interstitial phases on a rate of recovery and mobility of recrystallization front, significantly influences kinetics of static recrystallization of studied steels. On the other hand, Somani *et al.* **[67]** analyzed the Nb effect on SRX of TWIP steels. They concluded that SRX in high-Mn steels is markedly slower than in low-Mn carbon steels, and Nb presence significantly slows down the rate of SRX in both steels. Thus, the Nb effect is less pronounced when high Mn levels are present. Despite these results, in a previous study of microalloyed Nb TWIP steels Hamada *et al.* **[68]** determined that the lower the Nb alloying presence as precipitated

particles, the better the hot ductility presented. And the most important variables to control de hot ductility of TWIP steels are the grain size and strain hardening. Consequently, for microalloyed high-Mn TWIP steels of this research work the chemical composition and the interaction of alloying elements with temperature and strain rate, are the main factors controlling the operative deformation mechanisms.

4.7. Microstructural evolution.

The microstructural evolution of the studied microalloyed TWIP steels was analyzed by using the generated orientation imaging microscopy (OIM) maps. The high angle boundaries (misorientations>15º) and low angle boundaries (misorientations<15º) are shown as black and white lines, respectively (**Figs. 8** and **9**). Additionally, the different coincidence site lattice (CSL) relationships are marked with different colors. Σ3 twin (misorientation of 60º about a <111> axis), Σ9 and Σ27 boundaries are shown as red, blue and yellow lines, respectively. The quantitative method performed to determine the recrystallized grains was the grain average misorientation (GAM), which analyzes the average misorientation between all neighboring pairs of points in a grain **[69, 70]**. In the present research work, the GAM by consideration of a threshold value of 1.55º was used to distinguish between recrystallized and deformed grains. Grains with GAM less than 1.55º were considered as recrystallized grains. The considered GAM criteria was used successfully for austenitic stainless steels by Mirzadeh *et al.* **[71]** and for TWIP steels by Reyes-Salas *et al.* **[72]**.

Fig. 8 shows the EBSD maps of the microstructural evolution during hot deformation of TW-NM steel tested at 1100 ºC and 10^{-4} s^{-1} (**Figs. 8** (**a**, **b**, and **c**)), and tested at 900 ºC and 10^{-1} s^{-1} (**Figs. 8** (**d**, **e**, and **f**)). **Figs. 8** (**a**, and **d**) show the microstructure maps with band contrast (BC), which in turn allows to visualize clearly the present microstructure, as well as the grain boundaries (GB) (thick black lines) and sub-grains (thin white lines). The results indicate that the higher the test temperature the higher the heterogeneous grain size (**Fig. 8**(**a**)). This is also an evidence of dynamically recrystallized grains. The resulting grains are larger because of the test duration. The TW-NM steel tested at lower temperature (**Fig. 8**(**d**)) shows heterogeneous grain size and the largest grains are oriented toward the flow direction. The largest grains are sub-structured and surrounded by the classical necklace effect (finer recrystallized grains).

Figs. 8(**b**, and **e**) show the CSL Σ3, Σ9 and Σ27. At high test temperature, the presence of CSL Σ3 forming multiple groups with the same orientation is higher into the deformed grains. Most of the CSL Σ9 and Σ27 are located close to the old grain boundaries, which is an evidence of changes in the crystal orientation (rotation) to become twins or new grain boundaries. In **Fig. 8**(**e**), twins (CSL Σ3) are only present into the new recrystallized grains and those located close the old grain boundaries have serrated morphology, which is appropriate for nucleate new austenitic grains. The deformed grains have no presence of annealing twins. This is in accordance with the results of Sakai *et al.* **[73]**, where there were neither deformation twins nor annealing twins into the deformed grains.

The EBSD maps in **Figs. 8** (**c**, and **f**) and **9** (**c**, and **f**) show the crystal orientations to the TW-NM and TW-Ti steels, respectively. The blue color corresponds to the recrystallized grains (GAM<1.55º), the red color to the deformed grains (GAM>1.55º) and the yellow color corresponds to the sub-structured grains (misorientation in the range of 10-15º). At high temperature only the 41% of grains were recrystallized, a few fraction of 1% remains deformed and the 58% is sub-structured, as shown in **Fig. 8**(**c**). For the TW-NM steel at 900 °C the necklace grains are composed by 37% of recrystallized grains, the sub-structured grains are the 9% fraction and the fraction of deformed grains is the 54% located around the largest deformed grains.

Fig. 9 shows the EBSD maps of deformed microstructures of TW-Ti steel. These grains are more deformed and elongated trough the flow direction than those presented to the TW-NM steel. The grain coarsening showed in **Fig. 9**(**a**) is due to the permanence at high temperature. There is a few percent of annealing twins (CSL Σ3), which are located randomly into the finest grains, as shown in **Fig. 9**(**b**). The largest sub-structured grains represent the highest volume fraction (51%), the recrystallized grains represent the 29% of volume fraction and the 21% remaining corresponds to deformed grains.

At high strain rate (10^{-1} s^{-1}) and low deformation temperature (900 ºC), the microstructure of TW-Ti steel displays deformed elongated grains surrounded by finer grains (**Figs. 9** (**d**, **e**, and **f**)), which is an indicative that these test conditions were insufficient to complete the DRX. The CSL Σ3, Σ9 and Σ27 are isolated into the microstructure (**Figs. 9** (**b**, and **e**)). The TW-Ti steel microstructure is more refined than the TW-NM steel at the same hot deformation condition. The recrystallized volume fraction (blue) is about 16%, the sub-structured grains

(yellow) represent the 9% of the volume fraction and the deformed grains volume (red) is the 75%, as is shown in **Fig. 9**(**f**).

During the steady-state stage, the stress remains constant and microstructure evolves. The most important value to describe the DRX phenomenon is the recrystallized grain size (d_{rec}), which is dependent of the σ_{ss} value. An appropriate correction proposed to the relationship of McQueen and Jonas **[74]**, has been established by Derby **[75]**:

$$K_D = \left(\frac{\sigma_{ss}}{\mu}\right)\left(\frac{d_{rec}}{b}\right)^{n_D} \tag{22}$$

where K_D is the Derby's coefficient, whose values are between 1 and 10; n_D is the Derby's exponent, which is commonly n_D=2/3; μ_0 is the shear modulus and b is the Burger's vector. **Fig. 10** shows that two of the four present steels (TW-NM and TW-Nb) are in good agreement with the Derby's equation, because n_D exponent has close values to 2/3, while in the other two steels (TW-V and TW-Ti) n_D=1/3. According to equation (22), a large recrystallized grain size indicates a low σ_{ss} value. The TW-NM steel exhibited the largest recrystallized grain size at high temperature and low strain rate, as shown in **Fig. 10**(**b**). On the other hand, it is evident the grain size growth inhibition produced by microalloying elements such as V and Ti on hot deformation, which is showed by the low slopes of **Figs. 10**(**a**, and **b**).

5. Conclusions

1. The hot compression tests carried out to the studied TWIP steels allowed to determine the most important flow characteristics and the DRX onset, promoted by single peak curves.
2. Addition of Ti, V and Nb microalloying elements to TWIP steel produced a slight increase of peak stress (σ_p).
3. The DRX onset for the studied TWIP steels was delayed in tests carried out at 900 ºC, accompanied by an increase of peak strain (ε_p). The softening effect promoted by DRV and DRX was more evident at high temperatures (1000 and 1100 ºC) and low strain rate (10^{-4} s^{-1}), particularly in the TW-NM and TW-Nb steels.
4. A decrease on the activation energy required to recrystallization (Q_t) due to the microalloying elements addition was determined in the following order: *i*) TW-NM steel,

ii) TW-Ti steel, *iii*) TW-V steel and *iv*) TW-Nb steel. Likewise, the necessary time for 50% of recrystallization ($t_{50\%}$) was determined in the following order: *i*) TW-V, *ii*) TW-Ti and *iii*) TW-NM and *iv*) TW-Nb.

5. The good agreement between the experimental and predicted hot flow curves demonstrates that the constitutive equations predict with reasonable accuracy the hot flow behavior of the present TWIP steels. The short deviations presented at high temperature and high strain rates are attributable to experimental error conditions.
6. The addition of V and Ti to TWIP steel was more effective in the austenite grain growth control compared to that obtained in TW-NM and TW-Nb steels during hot deformation.

Acknowledgments

I. Mejía would like to thank the National Council on Science and Technology (Consejo Nacional de Ciencia y Tecnología-México) for the support during the project CB-2012-01-0177572. The present research project was also supported by the Coordinación de la Investigación Científica-UMSNH (México) (CIC-1.8), the Universitat Politècnica de Catalunya (Spain) and the Fundació CTM Centre Tecnològic (Spain). Authors want to give special thanks to Dr. Ahmed Boulaajaj, Dr. Pablo Rodríguez Calvillo and Dr. Oscar Fabián Higuera Cobos from Fundació CTM and UPC, for the technical support in hot compression tests, SEM-EBSD tests and EBSD data analysis. F. Reyes-Calderon wants to thank the financial support received from National Council on Science and Technology (Consejo Nacional de Ciencia y Tecnología-México, N.B. 30754).

References

[1] O. Grässel, L. Krüger, G. Frommeyer, L.W. Meyer, Int. J. Plasticity 16 (2000) 1392-1409.

[2] D. Barbier, N. Gey, S. Allain, N. Bozzolo, M. Humbert, Mater. Sci. Eng. A 500 (2009) 196-206.

[3] S. Vercammen, B. Blanpain, B.C. De Cooman, P. Wollants, Acta Mater. 52 (2004);: 2005-2012.

[4] S. Allain, J.P. Chateau, O. Bouaziz, S. Migot, N. Guelton, Mater. Sci. Eng. A 387-389 (2004) 158-162.

[5] P. Yang, Q. Xie, L. Meng, H. Ding, Z. Tang, Scr. Mater. 55 (2006) 629-631.

[6] A.S. Hamada, L.P. Karjalainen, M.C. Somani, Mater. Sci. Eng. A 467 (2007) 114-124.

[7] D. Li, Y. Feng, Z. Yin, F. Shangguan, K. Wang, Q. Liu, F. Hu, Mater. Sci. Eng. A 528 (2011) 8084-8089.

[8] D. Li, Y. Feng, Z. Yin, F. Shangguan, K. Wang, Q. Liu, Mater. Des. 34 (2012) 713-718.

[9] L.A. Dobrzański, A. Grajcar, W. Borek, JAMME 29 (2008) 139-142.

[10] L.A. Dobrzański, A. Grajcar, W. Borek, JAMME 31 (2008) 7-14.

[11] L.A. Dobrzański, W. Borek, JAMME 37 (2009) 397-407.

[12] L.A. Dobrzański, W. Borek, JAMME 40 (2010) 25-32.

[13] L.A. Dobrzański, W. Borek, JAMME 46 (2011) 71-78.

[14] M.O. Spíndola, E.A. Ribeiro, B.M. González, D.B. Santos, Rev. Mater. 15 (2010) 143-150.

[15] Y. Estrin, H. Mecking, Acta Metall. 32 (1984) 57-70.

[16] Y. Bergström, Mater. Sci. Eng. 5 (1970) 193-200.

[17] A.N. Kolmogorov, Izv. Akad. Nauk SSSR 3 (1937) 355-359.

[18] W.A. Johnson, R.F. Mehl, Trans. Metall. Soc. AIME 135 (1939) 416-458.

[19] M. Avrami, J. Chem. Phys. 7 (1939) 1103-1112.

[20] M. Avrami, J. Chem. Phys. 8 (1940) 212-224.

[21] M. Avrami, J. Chem. Phys. 9 (1941) 177-184.

[22] C.M. Sellars, W.J. McG. Tegart, Mem. Sci. Rev. Met. 63 (1966) 741-746.

[23] J.M. Cabrera, A. Al-Omar, J.M. Prado, J.J. Jonas, Metall. Mater. Trans. A 28 (1997) 2233-2244.

[24] B. Ralph, Mater. Sci. Technol. 6 (1990) 1136-1144.

[25] I. Mejía, E. López-Chipres, C. Maldonado, A. Bedolla-Jacuinde, J.M. Cabrera, Int. J. Mater. Res. 99 (2008) 1336-1345.

[26] J.J. Jonas, C.M. Sellars, W.J. McG. Tegart, Metall. Rev. 14 (1969) 1-24.

[27] C.M. Sellars, W.J. McG. Tegart, Acta Metall. 14 (1966) 1136-1138.

[28] A. Laasraoui, J.J. Jonas, Metall. Trans. A 22 (1991) 1545-1558.

[29] M. El-Wahabi, J.M. Cabrera, J.M. Prado, Mater. Sci. Eng. A 343 (2003) 116-125.

[30] Y.C. Lin, G. Liu, Comput. Mater. Sci. 48 (2010) 54-58.

[31] J.H. Sung, J.H. Kim, R.H. Wagoner, Int. J. Plasticity 26 (2010) 1746-1771.

[32] A. Momeni, K. Dehghani, Mater. Sci. Eng. A 527 (2010) 5467-5473.

[33] J. Zhang, H. Di, X. Wang, Y. Cao, J. Zhang, T. Ma, Mater. Des. 44 (2013) 354-364.

[34] D. Samantaray, S. Mandal, A.K. Bhaduri, Mater. Des. 31 (2010) 981-984.

[35] S. Mandal, V. Rakesh, P.V. Sivaprasad, S. Venugopal, K.V. Kasiviswanathan, Mater. Sci. Eng. A 500 (2009) 114-121.

[36] Y.H. Xiao, C. Guo, Mater. Sci. Eng. A 528 (2011) 5081-5087.

[37] M. Mirzaee, H. Keshmiri, G.R. Ebrahimi, A. Momeni, Mater. Sci. Eng. A 551 (2012) 25-31.

[38] S. Serajzadeh, A. Karimi Taheri, Mater. Des. 23 (2002) 271-276.

[39] H. Mirzadeh, A. Najafizadeh, Mater. Sci. Eng. A 527 (2010) 1856-1860.

[40] M.H. Wang, Y.F. Li, W.H. Wang, J. Zhou, A. Chiba, Mater. Des. 45 (2013) 384-392.

[41] A. Soulami, K.S. Choi, Y.F. Shen, W.N. Liu, X. Sun, M.A. Khaleel, Mater. Sci. Eng. A 528 (2011) 1402-1408.

[42] C.M, Sellars, Mater. Sci. Technol. 6 (1990) 1072-1081.

[43] C. Devadas, I.V. Samarasekera, E.B. Hawbolt, Metall. Trans. A 22 (1991) 335-349.

[44] F. Garofalo, Trans. Metall. Soc. AIME 227 (1963) 351-357.

[45] H.J. Frost, M.F. Ashby, Deformation-Mechanism Maps: The Plasticity and Creep of Metals and Ceramics, Pergamon Press, Oxford, 1982.

[46] ASTM E112-13, Standard Test Methods for Determining Average Grain Size, ASTM International, West Conshohocken, PA, 2013, www.astm.org. DOI: 10.1520/E0112.

[47] J.M. Cabrera, J.M. Prado, M.A. Barrón, Steel Res. Int. 70 (1999) 59-66.

[48] F. Reyes-Calderón, I. Mejía, J.M. Cabrera, Mater. Sci. Eng. A 562 (2013) 46-52.

[49] I. Mejía, G. Altamirano, A. Bedolla-Jacuinde, J.M. Cabrera, Mater. Sci. Eng. A 610 (2014) 116-125.

[50] D.A. Porter, K.E. Easterling, M.Y. Sherif, Phase Transformations in Metals and Alloys, third ed., Chapman & Hall, London, 2009.

[51] J.W. Christian, The Theory of Transformations in Metals and Alloys, third ed., Pergamon, Oxford, 2002.

[52] C.A. Hernandez, S.F. Medina, J. Ruiz, Acta Mater. 44 (1996) 155-163.

[53] S. Nanba, M. Kitamura, M. Shimada, M. Katsumata, T. Inoue, H. Imamura, Y. Maeda, S. Hattori, ISIJ Int. 32 (1992) 377-386.

[54] G. Anan, S. Nakajima, M. Miyahara, S. Nanba, M. Umemoto, A. Hiramatsu, A. Moriya, T. Watanabe, ISIJ Int. 32 (1992) 261-266.

[55] T. Sakai, A. Belyakov, H. Miura, in: G. Gottstein, D.A. Molodov (Eds.), Proceedings of the First Joint International Conference on Recrystallization and Grain Growth, Springer-Verlag, Aachen, Germany, 2001, pp. 669–682.

[56] N.X. Sun, X.D. Liu, K. Lu, Scr. Mater. 34 (1996) 1201-1207.

[57] I. Gutierrez-Urrutia, D. Raabe, Acta Mater. 59 (2011) 6449-6462.

[58] I. Gutierrez-Urrutia, S. Zaefferer, D. Raabe, Scr. Mater. 61 (2009) 737-740.

[59] D.R. Steinmetz, T. Jäpel, B. Wietbrock, P. Eisenlohr, I. Gutierrez-Urrutia, A. Saeed-Akbari, T. Hickel, F. Roters, D. Raabe, Acta Mater. 61 (2013) 494-510.

[60] X.H. Fang, P. Yang, F.Y. Lu, L. Meng, J. Iron Steel Res. Int. 18 (2011) 46-52.

[61] L.J. Cuddy, Metall. Trans. A 12 (1981) 1313-1320.

[62] L.J. Cuddy, in: A.J. DeArdo, G.H. Ratz and P.J. Wray (Eds.), TMS-AIME, Warrendale, PA, 1982, pp. 129-139.

[63] L.J. Cuddy, Metall. Trans. A 15 (1984) 87-98.

[64] S. Vervynckt, K. Verbeken, P. Thibaux, M. Liebeherr, Y. Houbaert, ISIJ Int. 49 (2009) 911-920.

[65] J. Speer, S. Hansen, Metall. Mater. Trans. A 20 (1989) 25-38.

[66] M. Opiela, W. Ozgowicz, JAMME 55 (2012) 759-771.

[67] M.C. Somani, H. Tervonen, L.P. Karjalainen, D.A. Porter, Mater. Sci. Forum 753 (2013) 195-200.

[68] A.S. Hamada, L.P. Karjalainen, Mater. Sci. Eng. A 528 (2011) 1819-1827.

[69] S. Mitsche, P. Poelt, C. Sommitsch, J. Microsc. 227 (2007) 267-274.

[70] R.J. McCabe, D.F. Teter, J. Microsc. 223 (2006) 33-39.

[71] H. Mirzadeh, J.M. Cabrera, A. Najafizadeh, P.R. Calvillo, Mater. Sci. Eng. A 538 (2012) 236-245.

[72] A.E. Salas-Reyes, I. Mejía, A. Bedolla-Jacuinde, A. Boulaajaj, J. Calvo, J.M. Cabrera, Mater. Sci. Eng. A 611 (2014) 77-89.

[73] T. Sakai, J.J. Jonas, Acta Metall. 32 (1984) 189-209.

[74] H.J. McQueen, J.J. Jonas, in: R.J. Arsenault (Ed.), Plastic Deformation of Materials, Academic Press, New York, 1975, pp. 393-493.

[75] B. Derby, Scr. Metall. Mater. 27 (1992)1581-1585.

Table captions

Table 1. Chemical compositions (wt%) of the four analyzed TWIP steels.

Table 2. Constants derived from **Eq.** (**21**) to obtain $t_{50\%}$.

Table 3. Parameters calculated in the modeling procedure applied for TW-NM, TW-Nb, TW-V and TW-Ti steels.

Figure captions

Fig. 1. TWIP steels as-solution condition (initial grain size): a) TW-NM, b) TW-Nb, c) TW-V and d) TW-Ti.

Fig. 2. Hot flow curves of TWIP steels analyzed at three temperatures (900, 1000 and 1100 ºC) and constant strain rates of 10^{-1}, 10^{-2}, 10^{-3}, and 10^{-4} s^{-1}.

Fig. 3. Determination of a) Softening coefficients (Ω) vs. Z and b) Hardening coefficients (U) vs. Z, of analyzed TWIP steels.

Fig. 4. Dependence of a) Peak stress (σ_p) and b) Peak strain (ε_p), on the Zener-Hollomon parameter (Z).

Fig. 5. Calculations of Avrami's coefficient: a) ln(ln(1/(1-X))) vs. ln((ε-ε_p)/$\dot{\varepsilon}$) plot to obtain n and K at 900ºC of TW-NM steel, and b) n vs. Z, of analyzed TWIP steels.

Fig. 6. a) Evolution of $(\dot{\varepsilon}/D_{Fe}^{\gamma}(T))^{1/5}$ vs. ($\sigma_p/E(T)$), and b) Evolution of $(\dot{\varepsilon}/D_{Fe}^{\gamma}(T))^{1/5}$ vs. ($\sigma_{ss}/E(T)$) of TW-NM steel and the determined curves by hyperbolic sine fitting.

Fig. 7. Comparison of the experimental (solid) and predicted (symbols) flow stress curves of microalloyed TWIP steels at 900, 1000 and 1100 ºC and four strain rates (10^{-4}, 10^{-3}, 10^{-2} and 10^{-1} s^{-1}).

Fig. 8. EBSD maps of the microstructural evolution of TW-NM steel deformed at T=1100 ºC and $\dot{\varepsilon}=10^{-4}$ s^{-1}, a) BC+GB, b) BC+GB+CSL, c) BC+GB+RF; and deformed at T= 900 ºC and $\dot{\varepsilon}=10^{-1}$ s^{-1}, d) BC+GB, e) BC+GB+CSL, f) BC+GB+RF.

Fig. 9. EBSD maps of the microstructural evolution of TW-Ti steel deformed at T=1100 ºC and $\dot{\varepsilon}=10^{-4}$ s^{-1}, a) BC+GB, b) BC+GB+CSL, c) BC+GB+RF; and deformed at T=900 ºC and $\dot{\varepsilon}=10^{-1}$ s^{-1}, d) BC+GB, e) BC+GB+CSL, f) BC+GB+RF.

Fig. 10. a) Relationship between σ_{ss} normalized by shear modulus (μ_0), and the recrystallized grain size (d_{rec}) normalized by Burgers vector (b) to determine the Derby's constants (n y K); and b) Relationship between d_{rec} vs. Z.

Table 1. Chemical compositions (wt%) of the four analyzed TWIP steels.

TWIP steel	C	Mn	Al	Si	Nb	V	Ti	N	Fe
TW-NM	0.41	21.2	1.5	1.5	-	-	-	0.012	Bal.
TW-Nb	0.40	22.4	1.6	1.4	0.06	-	-	0.015	Bal.
TW-V	0.43	22.5	1.6	1.4	-	0.12	-	0.013	Bal.
TW-Ti	0.40	22.3	1.6	1.4	-	-	0.18	0.007	Bal.

Table 2. Constants derived from **Eq.** (**21**) to obtain $t_{50\%}$.

TWIP steel	$k_{t50\%}$	$m_{t50\%}$	Q_t (kJ/mol)	$t_{50\%}$ (s)	Adj. R^2
TW-NM	0.0062	-1.1024	27.44	11.09	0.98
TW-Nb	0.1222	-1.0164	8.64	2.7	0.99
TW-V	0.0725	-1.0706	9.03	3,067.27	0.95
TW-Ti	0.0364	-1.0819	12.29	2,274.81	0.92

Table 3. Parameters calculated in the modeling procedure applied for TW-NM, TW-Nb, TW-V and TW-Ti steels.

Modeling stage	Parameter	TWIP Steel			
		TW-NM	**TW-Nb**	**TW-V**	**TW-Ti**
I. Softening (Ω)	K_Ω	2.37E3	3.81E3	1.01E5	1.09E6
$\Omega = K_\Omega \cdot Z^{m_\Omega}$	m_Ω	-0.15	-0.14	-0.22	-0.31
II. Hardening (U)	K_U	3.19E3	5.8E2	9.36E3	3.11E4
$(\alpha' \mu b)^2 \cdot U = K_U \cdot Z^{m_U}$	m_U	0.15	0.17	0.09	0.07
III. Peak strain (ε_p)	$K_{\varepsilon p}$	1.89E-2	6.9E-3	1.5E-3	1.06E-2
$\varepsilon_p = K_\varepsilon . Z^{m_\varepsilon}$	$m_{\varepsilon p}$	0.08	0.1	0.13	0.09
IV. Avrami's exponent (n_A)	a	1.13	0.79	2.31	3.01
$n_A = a + b \cdot log\ Z$	b	6.3E-3	0.01	-0.02	-0.05
V. Time for 50%-DRX ($t_{50\%}$)	$k_{t50\%}$	6.25E-3	0.12	0.07	0.03
	$m_{t50\%}$	-1.1	-1.01	-1.07	-1.08
$t_{50\%} = k_{t50\%} \cdot \dot{\varepsilon}^{m_{t50\%}} \cdot exp\left(\frac{Q_t}{RT}\right)$	Q_t (kJ/mol)	27.44	8.64	9.03	12.29
	Adj. R^2	0.98	0.99	0.95	0.92
VI. Peak stress (σ_p)	A_p	7.99E2	1.01E3	4.98E2	5.41E2
$\frac{\dot{\varepsilon}}{D_{Fe}^{\gamma}(T)} = A_p \left[\sinh\left(\frac{\alpha_p \sigma_p}{E(T)}\right)\right]^5$	α_p	8.97E8	7.12E8	1.21E9	1.12E9
VII. Steady-state stress (σ_{ss})	A_{ss}	1.33E3	1.56E3	7.79E2	6.83E2
$\frac{\dot{\varepsilon}}{D_{Fe}^{\gamma}(T)} = A_{ss} \left[\sinh\left(\frac{\alpha_{ss} \sigma_{ss}}{E(T)}\right)\right]^5$	α_{ss}	6.62E8	5.41E8	9.83E8	1.01E9

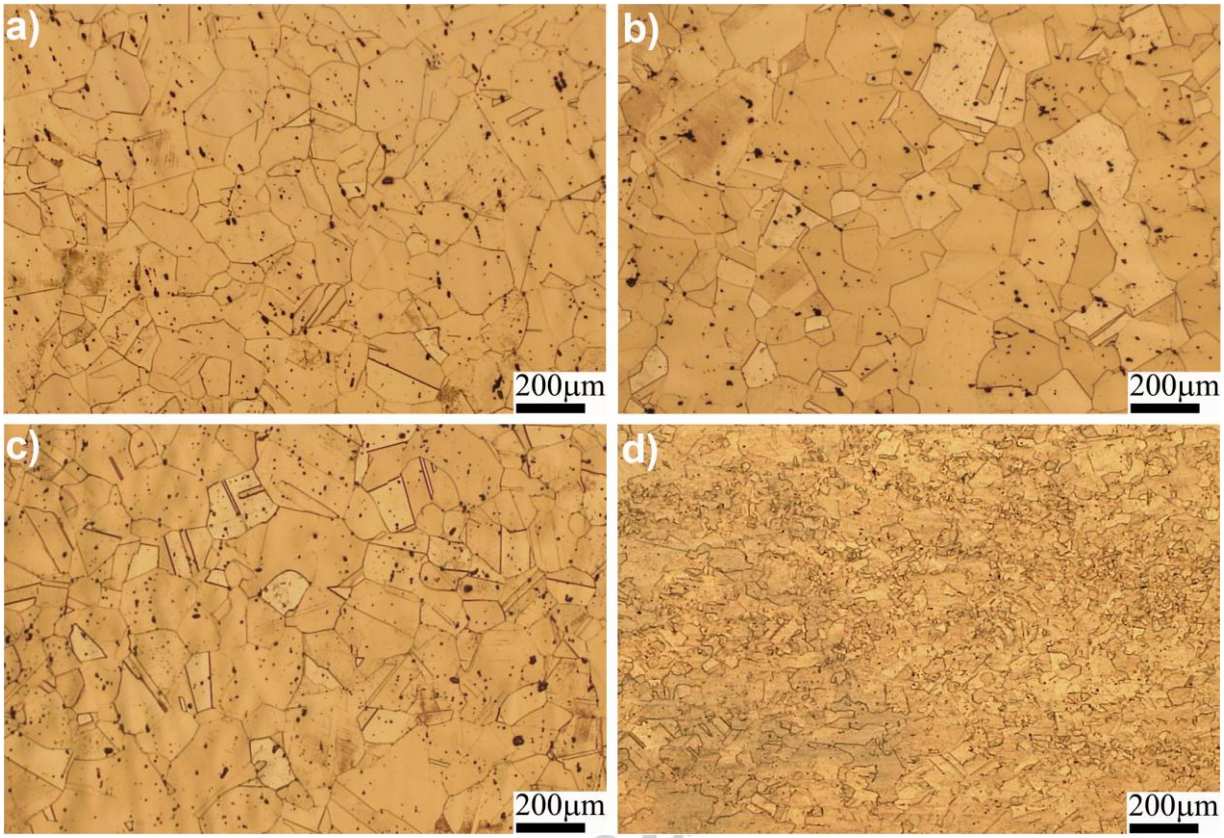

Fig. 1. TWIP steels as-solution condition (initial grain size): a) TW-NM, b) TW-Nb, c) TW-V and d) TW-Ti.

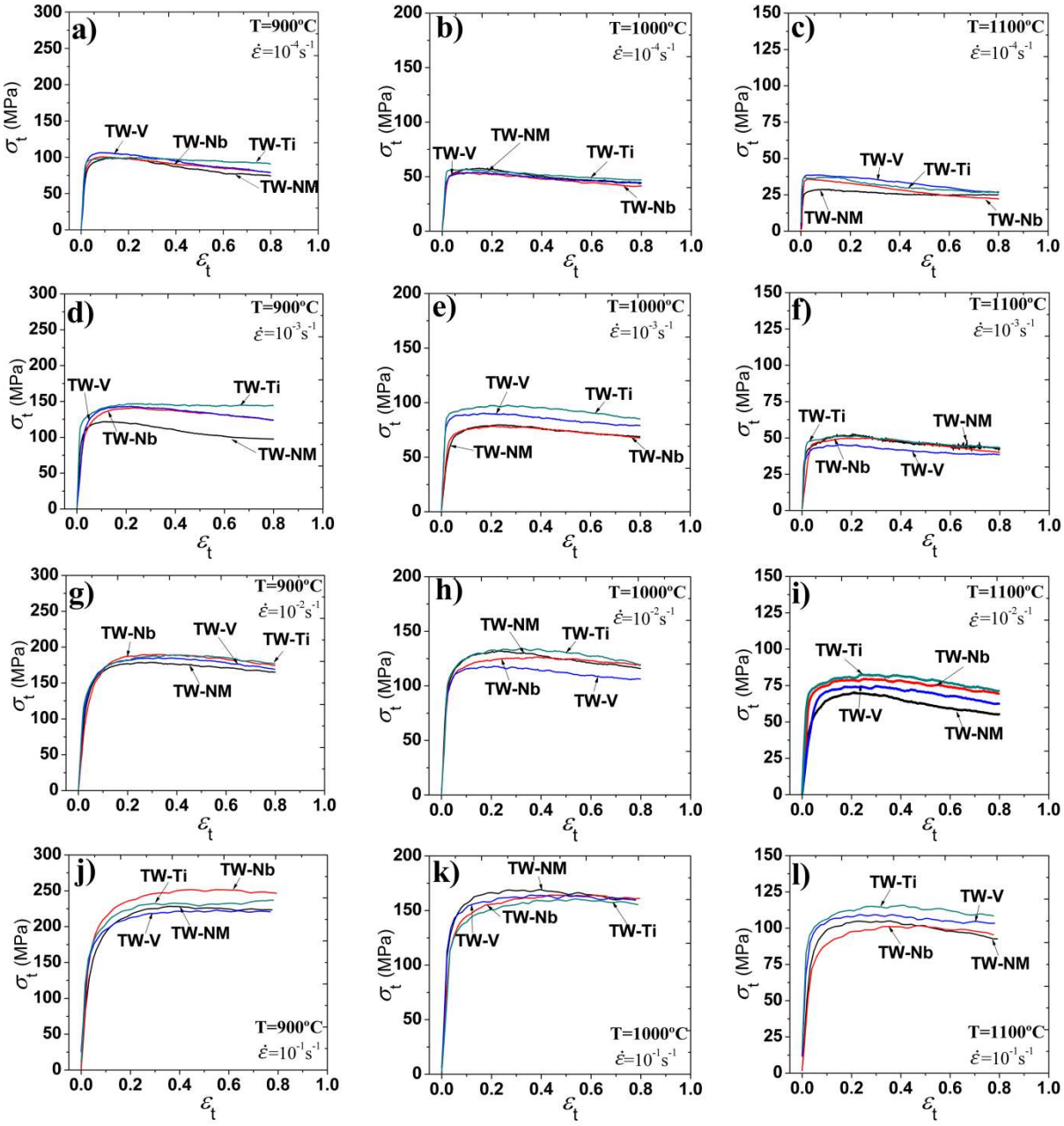

Fig. 2. Hot flow curves of TWIP steels analyzed at three temperatures (900, 1000 and 1100 ºC) and constant strain rates of 10^{-1}, 10^{-2}, 10^{-3}, and 10^{-4} s^{-1}.

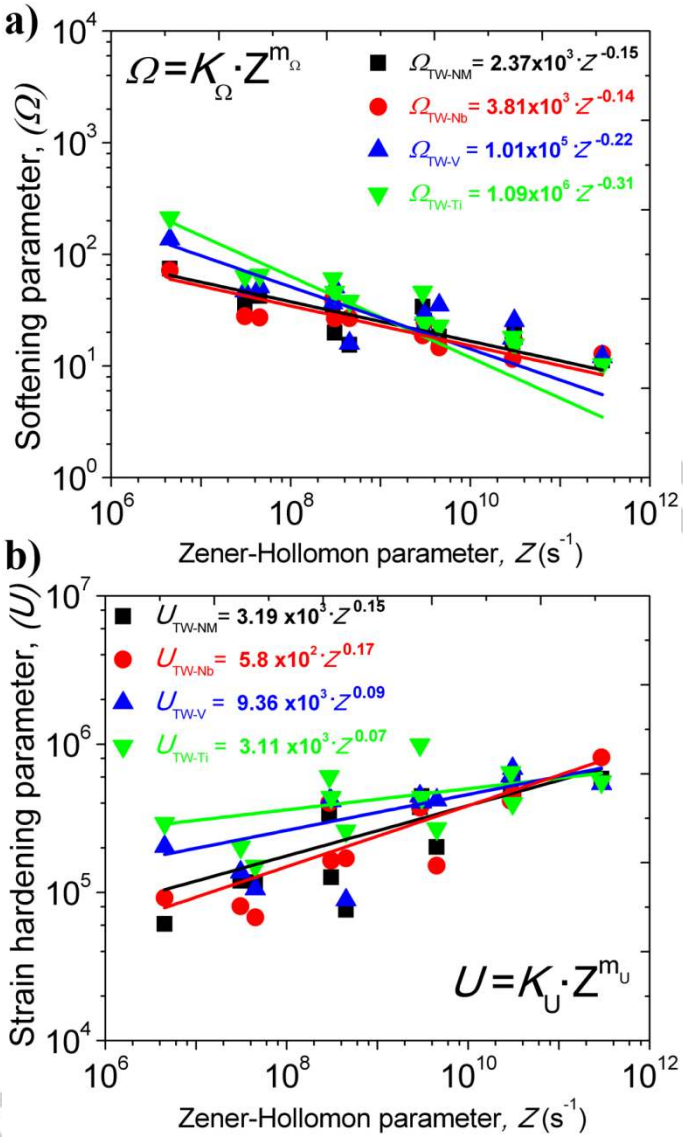

Fig. 3. Determination of a) Softening coefficients (Ω) vs. Z and b) Hardening coefficients (U) vs. Z, of analyzed TWIP steels.

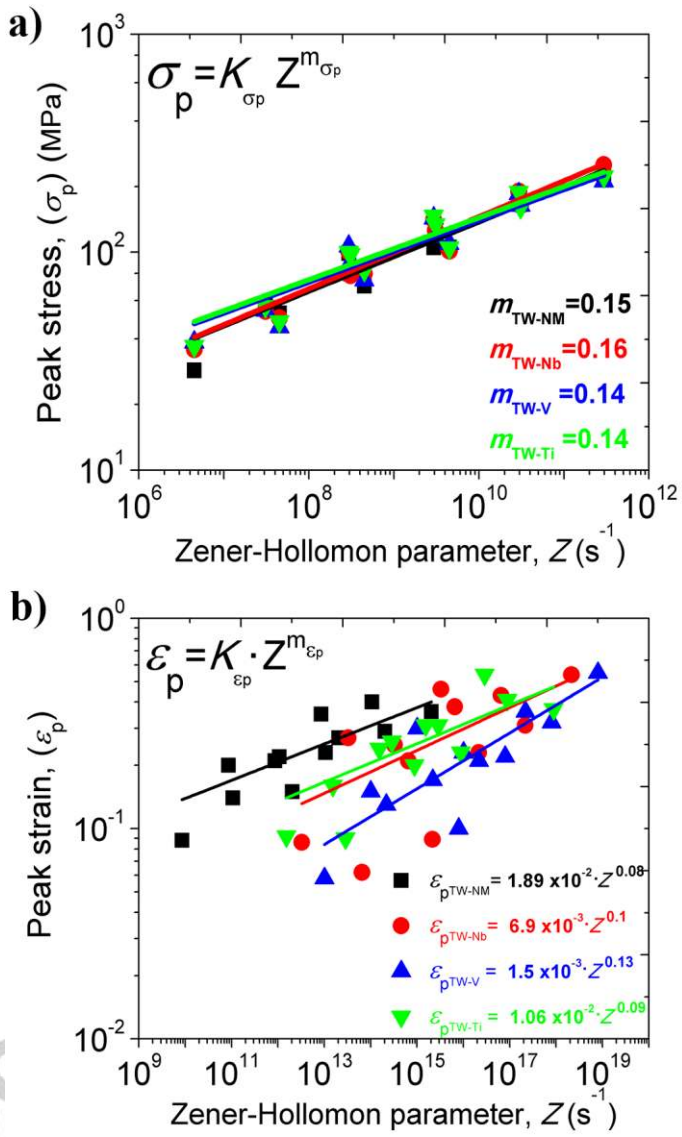

Fig. 4. Dependence of a) Peak stress (σ_p) and b) Peak strain (ε_p), on the Zener-Hollomon parameter (Z).

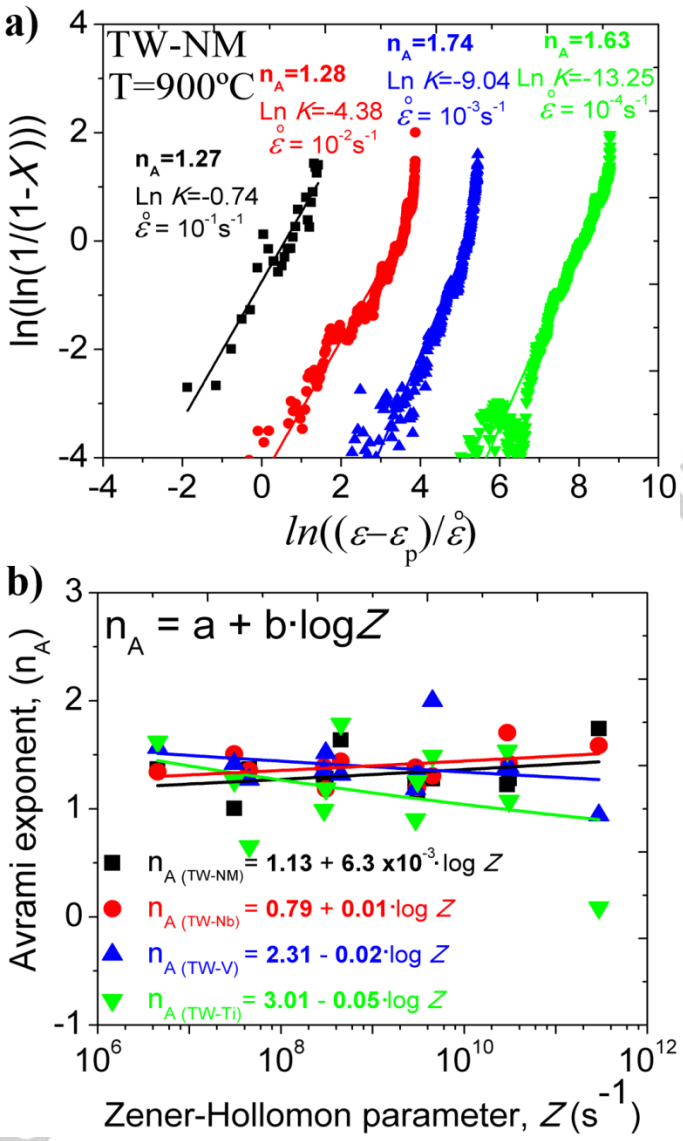

Fig. 5. Calculations of Avrami's coefficient: a) ln(ln(1/(1-*X*))) vs. ln((*ε*-*ε*$_p$)/$\dot{\varepsilon}$) plot to obtain *n* and *K* at 900 ºC of TW-NM steel, and b) *n* vs. Z, of analyzed TWIP steels.

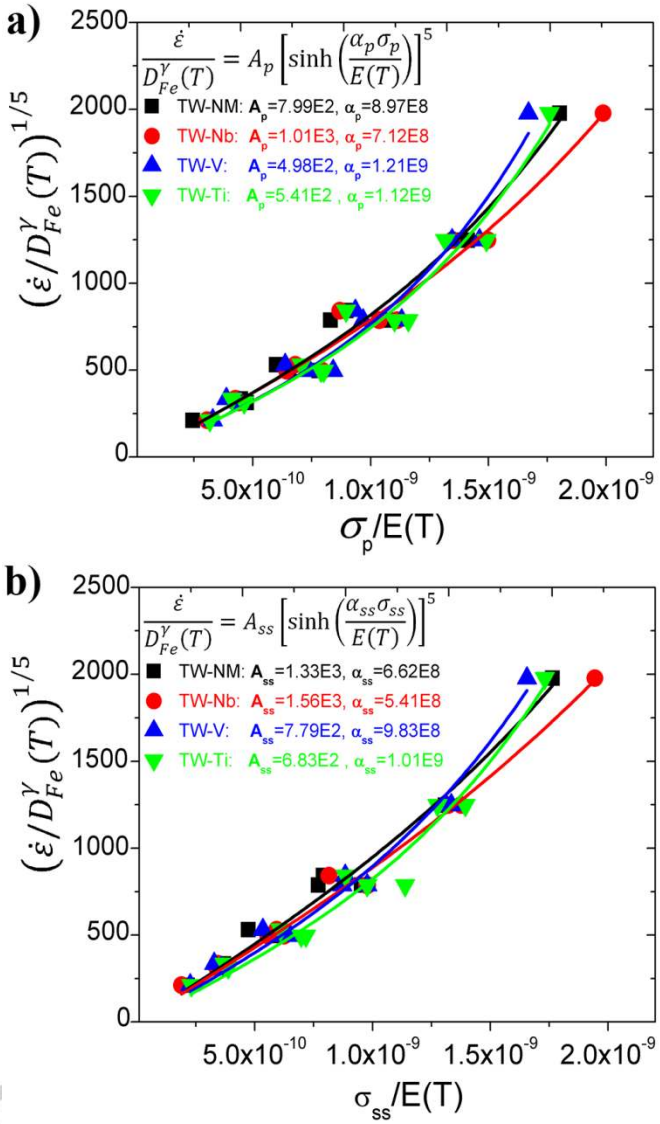

Fig. 6. a) Evolution of $(\dot{\varepsilon}/D_{Fe}^{\gamma}(T))^{1/5}$ vs. $(\sigma_p/E(T))$, and b) Evolution of $(\dot{\varepsilon}/D_{Fe}^{\gamma}(T))^{1/5}$ vs. $(\sigma_{ss}/E(T))$ of TW-NM steel and the determined curves by hyperbolic sine fitting.

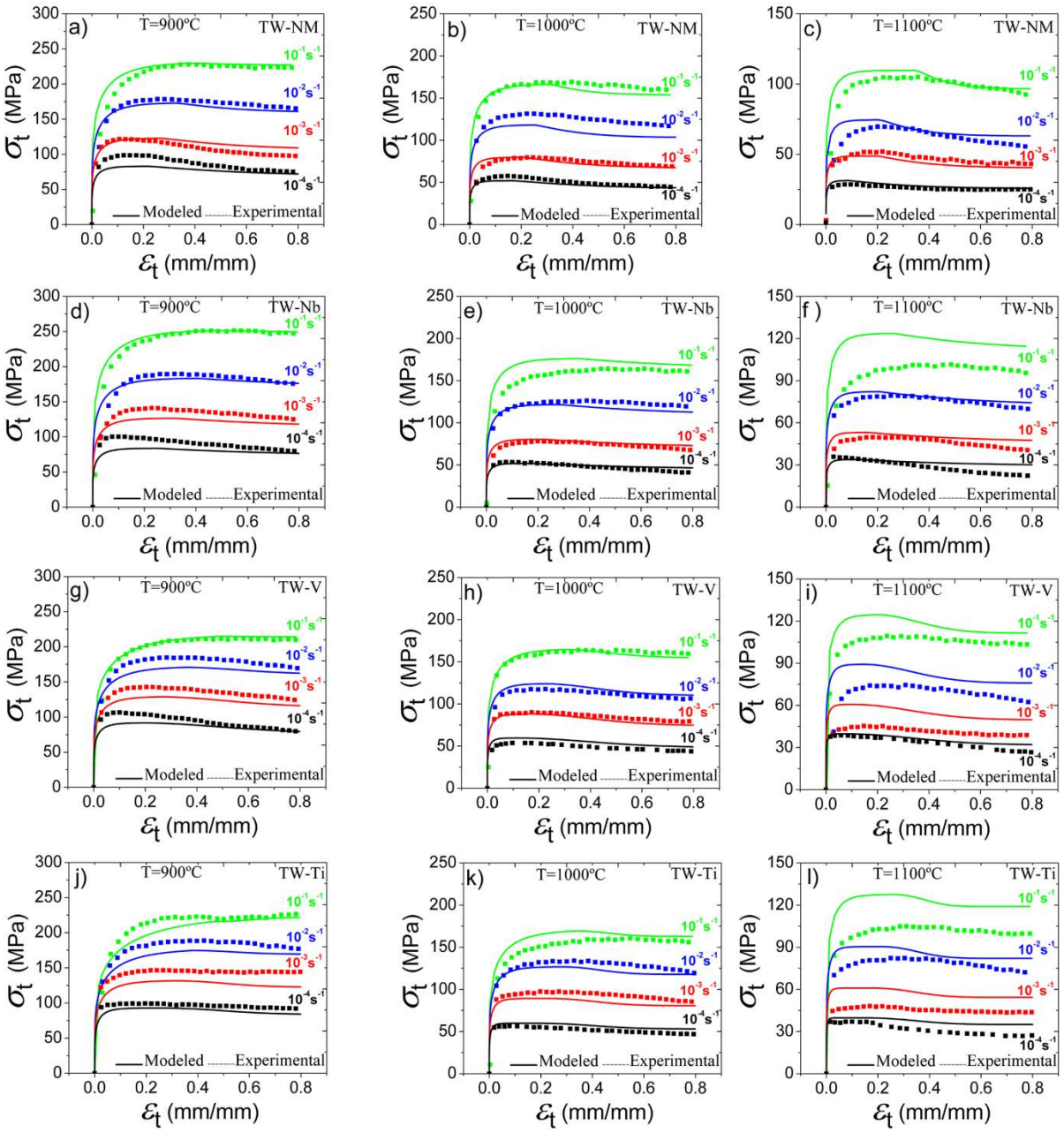

Fig. 7. Comparison of the experimental (solid) and predicted (symbols) flow stress curves of microalloyed TWIP steels at 900, 1000 and 1100 ºC and four strain rates (10^{-4}, 10^{-3}, 10^{-2} and 10^{-1} s^{-1}).

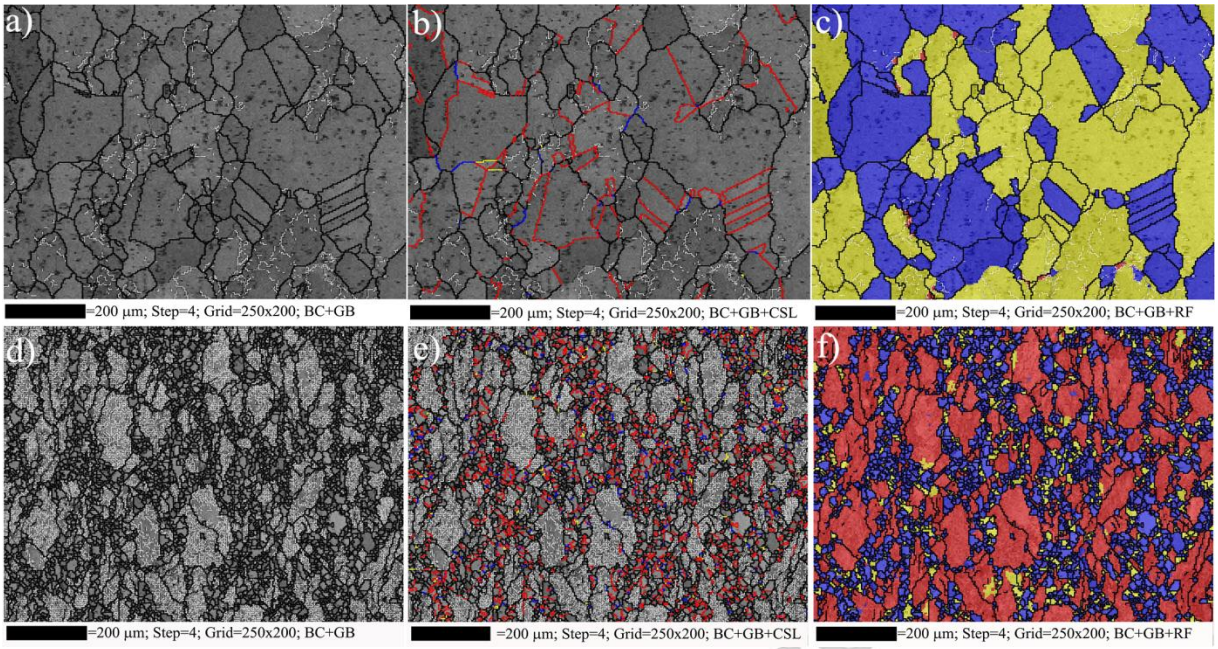

Fig. 8. EBSD maps of the microstructural evolution of TW-NM steel deformed at T=1100 ºC and $\dot{\varepsilon}=10^{-4}$ s^{-1}, a) BC+GB, b) BC+GB+CSL, c) BC+GB+RF; and deformed at T= 900 ºC and $\dot{\varepsilon}=10^{-1}$ s^{-1}, d) BC+GB, e) BC+GB+CSL, f) BC+GB+RF.

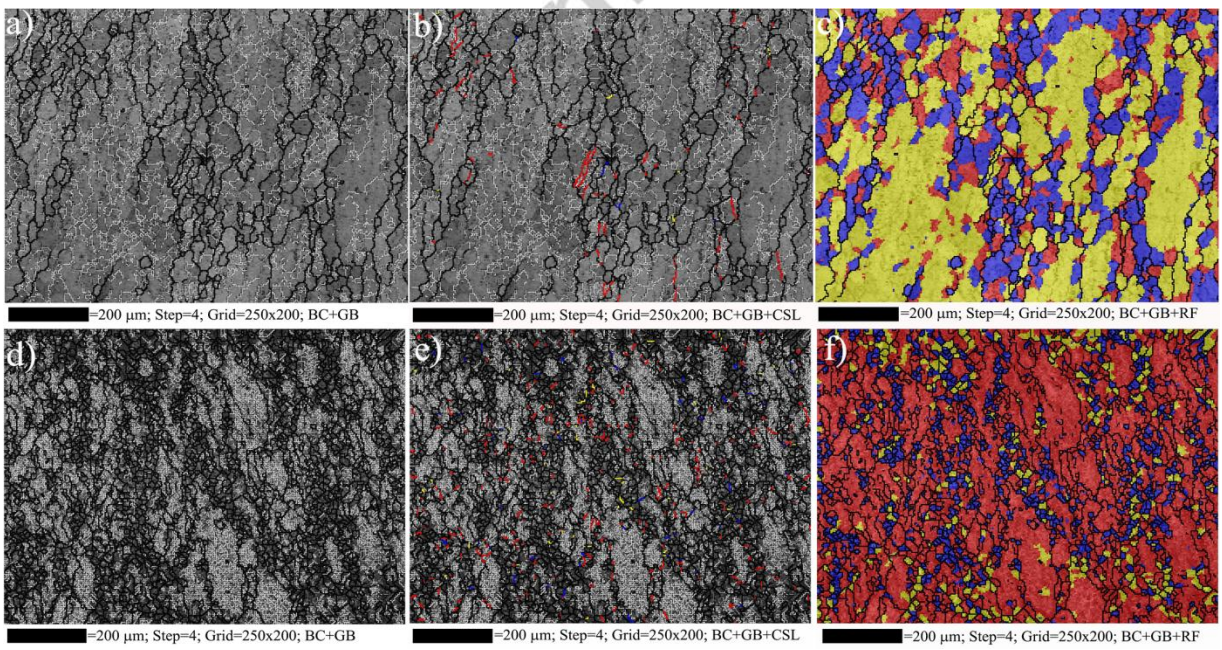

Fig. 9. EBSD maps of the microstructural evolution of TW-Ti steel deformed at T=1100 ºC and $\dot{\varepsilon}=10^{-4}$ s^{-1}, a) BC+GB, b) BC+GB+CSL, c) BC+GB+RF; and deformed at T=900 ºC and $\dot{\varepsilon}=10^{-1}$ s^{-1}, d) BC+GB, e) BC+GB+CSL, f) BC+GB+RF.

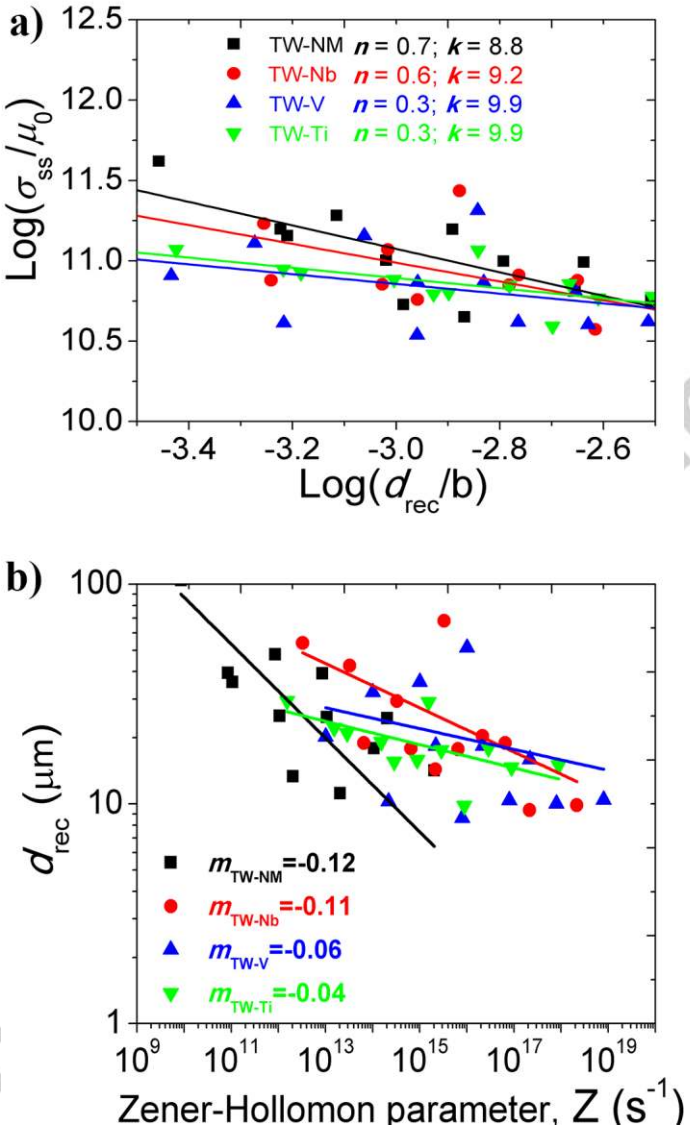

Fig. 10. a) Relationship between σ_{ss} normalized by shear modulus (μ_0), and the recrystallized grain size (d_{rec}) normalized by Burgers vector (b) to determine the Derby's constants (n y K); and b) Relationship between d_{rec} vs. Z.